Journal of Materials Chemistry A

ROYAL SOCIETY OF CHEMISTRY

PAPER

View Article Online
View Journal | View Issue

Check for updates

Cite this: J. Mater. Chem. A, 2025, 13, 39748

Achieving Pt-coating-free anodes using double-layered catalyst layer structure for polymer electrolyte membrane water electrolysis†

Daehee Kim,[ab] Gi Hong Jung,[a] Young Hwa Yun,[a] Jeesoo Park,[c] Sieon An,[a] Changsoo Lee,[a] Sechan Lee,[de] Hyeonjung Park,[a] Sang-Kyung Kim,[a] Hyun-Seok Cho,[f] Hee-Tak Kim,[c] Namgee Jung,*[b] Gisu Doo*[a] and MinJoong Kim*[g]

Received 28th February 2025
Accepted 4th May 2025

DOI: 10.1039/d5ta01688f

rsc.li/materials-a

Achieving high-performance and cost-effective proton exchange membrane water electrolysis (PEMWE) necessitates a reduction in the use of precious group metals (PGMs) while maintaining electrolysis efficiency. However, commercial high-activity IrO_x catalysts often fail to deliver optimal performance at low loadings because of electron transport problems caused by the natural oxide (TiO_x) on the Ti porous transport layer (PTL) surface. This is because the high work functions of IrO_x catalysts create Schottky barriers in the low-work-function TiO_x, thereby deteriorating the electrical conductivity at the interface. The Pt coating is commonly employed as a protective layer; however, hundreds of nanometers of coating significantly increase the cost of the electrolyzer. To address this challenge, we propose a double-layered catalyst layer (DL-CL) structure that enables the fabrication of Pt-coating-free anodes, with crystalline, low-work-function rutile IrO_2 (R-IrO_2) positioned at the PTL interface and highly active IrO_x (HA-IrO_x) positioned on the membrane side. The key advantage of the R-IrO_2 layer over the Pt coating is its porous structure, which effectively prevents contact between HA-IrO_x and TiO_x with much lower loading (0.05–0.2 mg cm^{-2}). The DL-CL minimizes the influence of TiO_x on both performance and durability while enabling all PGMs to actively participate in the oxygen evolution reaction.

1 Introduction

Hydrogen is a key component of next-generation energy systems and plays a crucial role in achieving carbon neutrality.[1–3] However, most hydrogen is still produced from fossil fuels, highlighting the need for efficient hydrogen production technologies linked to renewable energy sources.[4,5] Given this, proton exchange membrane water electrolysis (PEMWE) has attracted considerable attention owing to its numerous advantages, including high current density, high hydrogen purity, and excellent responsiveness to power fluctuations.[6,7] Nonetheless, there is a fatal drawback of high material cost, mainly due to platinum-group metals (PGMs) or titanium components that can withstand acidic environments and high anode potentials.[8–10]

One of the biggest contributions to the PEMWE cost is Pt coatings, which are currently employed to conceal the native oxide (TiO_x) of the titanium components.[11,12] For industrial uses, hundreds of nanometers of Pt, which is equivalent to 0.5–1 mg cm^{-2}, are coated on the Ti porous transport layer (PTL) and bipolar plate to enhance conductivity and corrosion resistance.[13–15] However, to achieve the ultimate hydrogen production cost target of 1 USD per kg, reducing PGM usage is essential, and the U.S. Department of Energy (DOE) has proposed an ultimate goal of 0.125 mg_{PGM} cm^{-2}.[16–18] This highlights the need to minimize or eliminate the Pt coatings, but significant challenges remain.[19,20]

Previous studies have pointed out the detrimental effects of TiO_x on both electrolyzer performance and durability.[13,21,22] In

[a]Hydrogen Research Department, Korea Institute of Energy Research (KIER), 152 Gajeong-ro, Yuseong-gu, Daejeon 34129, Republic of Korea. E-mail: dooanything@kier.re.kr

[b]Graduate School of Energy Science and Technology (GEST), Chungnam National University, 99 Daehak-ro, Yuseong-gu, Daejeon 34134, Republic of Korea. E-mail: njung@cnu.ac.kr

[c]Department of Chemical and Biomolecular Engineering, Korea Advanced Institute of Science and Technology (KAIST), 291 Daehak-ro, Yuseong-gu, Daejeon 34141, Republic of Korea

[d]Department of Chemistry, Kookmin University, 77 Jeongneung-ro, Seongbuk-gu, Seoul 02707, Republic of Korea

[e]Department of Applied Chemistry, Kookmin University, 77 Jeongneung-ro, Seongbuk-gu, Seoul 02707, Republic of Korea

[f]Department of Chemical and Biomolecular Engineering, Sogang University, 35 Baekbeom-ro, Mapo-gu, Seoul 04107, Republic of Korea

[g]Department of Materials Science and Engineering, Kyung Hee University, 1732 Deogyeong-daero, Giheung-gu, Yongin, Gyeonggi-do 17104, Republic of Korea. E-mail: mj.kim@khu.ac.kr

† Electronic supplementary information (ESI) available. See DOI: https://doi.org/10.1039/d5ta01688f

addition, a lower IrO_x loading in the anode intensifies the problems caused by TiO_x, that is, retardation of electron transport at the interface and deterioration of single-cell performance.[12,23,24] Many researchers have observed abnormally poor single-cell performance of low-IrO_x-loading anodes, mostly attributable to large ohmic polarization.[19,25,26] Our recent publications have ascribed these electron-transport problems to the semiconducting properties of TiO_x.[27] Specifically, the high work functions of the IrO_x catalysts and electron-withdrawing fluorinated ionomers result in electron depletion and upward band bending in the TiO_x, lowering the electrical conductivity at the interface.[27,28] Moreover, IrO_x catalysts with higher activities tend to have higher work functions, promoting band bending and increasing the interfacial resistance.[27,29,30] Because the low loading and high activity of IrO_x catalysts are some of the biggest challenges in achieving high-performance and cost-effective anodes, the problems caused by TiO_x are of great interest in PEMWE development.

Recently, our group focused on designing catalyst layer (CL) structures that can mitigate the abovementioned problems caused by TiO_x and realize a Pt-coating-free anode. Our previous studies concluded that porous and low-work-function CLs are necessary to prevent band bending at the TiO_x interface.[27] Based on this conclusion, we suggested that an Ir metal nanofiber is the ideal anode catalyst structure.[30] Owing to its high porosity and low work function, the Ir nanofiber CL effectively suppressed the problems caused by TiO_x, exhibiting the same performance regardless of the Pt coating. However, the nanofiber catalyst has limitations in the complex manufacturing process and relatively low catalytic activity, requiring additional strategies for practical industrial applications.[30,31]

Herein, we propose a double-layered CL (DL-CL) structure that enables the fabrication of Pt-coating-free anodes with high activity and a simple manufacturing process.[32] The DL-CL consists of two distinct layers of rutile IrO_2 (R-IrO_2) and highly amorphous IrO_x (HA-IrO_x) that face the Ti PTL and membrane, respectively. Because of its high crystallinity, low work function, and excellent electrochemical stability, thermally treated R-IrO_2 is introduced at the TiO_x interface to alleviate band bending in TiO_x.[21,33] However, since the R-IrO_2 catalyst inherently possesses low activities for oxygen evolution reaction (OER), its loading is minimized to 0.05–0.2 mg cm^{-2}, while the HA-IrO_x catalyst is employed to reduce activation polarization.

In this regard, the DL-CL structure offers two significant benefits: (1) the minimal layer of low-work-function R-IrO_2 effectively addresses interface electron transport issues, and (2) the highly active HA-IrO_x CL in direct contact with the membrane maximizes the OER performance.[34–37] Electrochemical analyses verify the outstanding single-cell performance of the DL-CL anodes, which retain both high activity and electrical conductivity regardless of the Pt coating on the PTL.[38] Additionally, the longevity of the excellent interface properties is demonstrated in a constant-current durability test, in which TiO_x does not cause an increase in ohmic resistance over 1000 h. We believe that this double-layer strategy represents a breakthrough in the development of high-performance and cost-effective PEMWE anodes.

2 Experimental section

2.1. Fabrication of the single-layered catalyst layer

All the CLs were prepared using a roll mill for slurry dispersion and subsequent blade casting. A commercial IrO_x catalyst from Tanaka Kikinzoku Kogyo (TKK) was used as the HA-IrO_x catalyst. For the R-IrO_2 catalyst, another commercial iridium oxide black (Alfa Aesar, Premion) was annealed to obtain a high-crystalline IrO_2 structure. The annealing was conducted at 500 °C in ambient air for 1 h, with a ramp rate of 5 °C min^{-1}.

In the case of cathode CLs, Pt/C (TEC10E50E, 46.9 wt% Pt, Tanaka Kikinzoku Kogyo) were utilized. All the CLs adopted a commercial Nafion ionomer solution (D2020, IEC = 1.05 mequiv. per g, Dupont) as a binder. The ionomer-to-carbon ratio of the cathode CLs was set to 1.0, whereas the ionomer content of the anode CLs was adjusted to 10 wt% of the total solid content. The solid components were dispersed in a mixed solution of *n*-propanol (NPA; Junsei Chemical) and deionized (DI) water using a roll mill with zirconia balls for 72 h. The uniformly dispersed slurry was coated on a polyimide (Kapton) film using a doctor blade and subsequently dried at a 50 °C hot plate. The Ir and Pt loadings were controlled to 0.50 mg_{Ir} cm^{-2} and 0.20 mg_{Pt} cm^{-2}, respectively.

2.2. Fabrication of catalyst-coated membranes (CCMs)

Catalyst-coated membranes (CCMs) were fabricated by transferring the anode and cathode CLs of 9 cm^2 onto a Nafion membrane (NRE 212, 50 μm, Dupont), followed by decal-transfer at 125 °C with 20 kgf cm^{-2} for 6 min. The CCMs were then assembled in a single-cell hardware with single-parallel-patterned Ti flow fields. Titanium-based materials were used for the anode PTL and bipolar plates (BPP), whereas carbon-based materials were employed for the cathode PTL. A titanium PTL (2GDL06N-025, 250 μm, Bekaert) and a carbon PTL with a microporous layer (JNTG30A3, 320 μm, JNT) were used as the anode and cathode, respectively. In addition, Pt-coated Ti PTL (2GDL06-025-BS02PT, 250 μm with a 200 nm Pt coating, Bekaert) was used to eliminate electron transport problems caused by the native TiO_x.

2.3. Double-layered CL (DL-CL) fabrication

To fabricate the DL-CL, the R-IrO_2 catalyst was spray-coated onto an HA-IrO_x CCM fabricated by the decal transfer process described in Section 2.2. The iridium loading of the HA-IrO_x CL was 0.30 mg_{Ir} cm^{-2}, while the R-IrO_2 coating was controlled to 0.2 mg_{Ir} cm^{-2}, resulting in a total iridium loading of 0.5 mg_{Ir} cm^{-2} for DL-CL. The R-IrO_2 slurry for spray coating was prepared by dispersing R-IrO_2 *via* bath sonication for 1 h. After the uniform dispersion slurry was loaded into an injector and coated onto the 80 °C-heated CCM using a spray coater. The loading ratios of the two catalysts were varied to determine the minimum amount of R-IrO_2 required for fabricating high-performance DL-CL. The total catalyst loading was set to 0.50 mg_{Ir} cm^{-2}, whereas the spray-coated R-IrO_2 content was changed from 0.20 to 0.05 mg_{Ir} cm^{-2}. Two CCMs with single-layered HA-IrO_x and R-IrO_x CLs directly spray-coated on the

Nafion membranes were also fabricated for comparison with the DL-CL.

2.4. Electrochemical single-cell analysis

Electrochemical analysis for the single cells was evaluated at 80 °C with the deionized (DI) water flow of 15 mL min^{-1}. All single cells were activated 20 times by cycling chronopotentiometry (CP) and linear sweep voltammetry (LSV) over 20 times. For the CP step, the current was held at 1 A cm^{-2} for 1 min, and the LSV step was conducted from the open-circuit voltage (OCV) to 1.8 V with a scan rate of 10 mV s^{-1}. After the activation, IV polarization curves were obtained at a current density range of 0.01–5.0 A cm^{-2} by maintaining each current step for 2 min and recording the steady-state voltage stability. Simultaneously, electrochemical impedance data were collected in the frequency range of 100 kHz to 100 mHz to break down the resistance components. To evaluate the durability of the anode, a DL-CL CCM using a thicker membrane (N115, 125 μm, Dupont) was prepared, and its anode, coupled with the bare Ti PTL, was subjected to a 1000 h durability test. A constant current density operation at 1 A cm^{-2} was applied throughout the operation. IV polarization and impedance analyses were conducted at six points of 70 h, 200 h, 350 h, 500 h, 750 h, and 1000 h to monitor degradation phenomena. Identical experiments were also performed using HA-IrO_x anodes with and without the Pt coating for comparison. All the electrochemical measurements were performed using a potentiostat (HCP-803; BioLogic Science Instruments). For the overpotential breakdown analysis, three overpotential components (kinetic, ohmic, and other) were extracted from the polarization curves based on Tafel plots and ohmic resistance. Detailed procedures for deconvoluting the voltage losses into kinetic, ohmic, and other-related components are provided in ESI Note 1.†

2.5. Characterization

The particle size and morphology of each catalyst were analyzed using field-emission transmission electron microscopy (FE-TEM) (F200, JEOL) at 200 kV. The geometric surface area and pore distribution were measured using Brunauer–Emmett–Teller (BET) analysis (3Flex, Micromeritics). The crystalline structure of each IrO_x catalyst was determined using X-ray diffraction (XRD) (SmartLab, RIGAKU), and the surface oxidation states were confirmed using X-ray photoelectron spectroscopy (XPS; K-alpha, Thermo VG Scientific). All the XPS spectra were calibrated to the sp^3 carbon peak of adventitious carbon (C 1s, 284.5 eV).[39,40] The interface properties within the anode components were investigated using a work function analysis obtained from ultraviolet photoelectron spectroscopy (UPS; Axis-Supra, Kratos). The structures of the CLs were examined using scanning electron microscopy (SEM) (Regulus 8220, Hitachi) at an accelerating voltage of 10.0 kV. All characterizations were conducted at the Analysis Center for Energy Research (ACER) at the Korea Institute of Energy Research (KIER).

For the *in situ* characterizations of the catalysts, X-ray absorption spectroscopy (XAS) of the Ir L3-edge (11 215 eV) was collected at the 7D beamlines of the Pohang Accelerator Laboratory (PAL) with a flux of 5×10^{12} photons per second at 300 mA and 2.5 GeV. The catalyst and Nafion dispersions were drop-coated onto MPL-coated carbon papers (JNTG30A3, JNT), which were subjected to the *in situ* analysis in a 0.5 M H_2SO_4 solution. The applied potentials were controlled at 1.0, 1.2, 1.4, 1.6, and 1.8 V *versus* a reversible hydrogen electrode (RHE). X-ray absorption near-edge structure (XANES) signals were measured in the fluorescence mode. Data fitting and analyses were conducted using the Athena and Artemis software.

3 Results and discussion

3.1. Catalyst properties and TiO_x effects

The single-cell performance of the PEMWE was significantly affected by the nanometer-thick native oxide (TiO_x) on the Ti PTL. This phenomenon has been reported in previous studies, revealing that the electrical properties of TiO_x depend significantly on the structural and material properties of the CL in contact.[27,30] Hence, the single-cell performance is not solely determined by the intrinsic activity of the catalysts but more considerably by the physical properties of the catalysts and/or CLs that govern the electron transport resistance at the TiO_x interface. However, because of the limited understanding of the TiO_x phenomena and the lack of strategies for overcoming them, this study aimed to deepen the insights into the TiO_x interface, design an improved electrode structure, and develop a durable, high-performance, Pt-coating-free anode.

First, to explore the TiO_x phenomenon, two iridium oxide catalysts with different physical properties were selected: a commercial amorphous catalyst with a high specific surface area (HA-IrO_x) and a heat-treated catalyst with high crystallinity (R-IrO_2). For the latter, another commercial amorphous iridium oxide (a-IrO_x) was annealed at 500 °C in the air condition (Fig. S1†). The morphologies and structures of the catalysts were compared by TEM, as shown in Fig. 1a and b. HA-IrO_x, with particle sizes ranging from 1 to 10 nm, exhibited a uniform contrast without any discernible crystalline pattern, demonstrating its amorphous structure. By contrast, R-IrO_2 exhibited much larger particle sizes, ranging from 10 to 100 nm, along with clear crystalline patterns. Comparison with a-IrO_x (Fig. S1a†) revealed that the annealing process reduced the surface roughness and clarified the interface between the particles, while increasing the overall particle size. Additionally, the crystalline patterns became evident after annealing, confirming the development of high crystallinity.

Material characterizations with BET, XPS, and XRD were in good agreement with the TEM images.[9,35,36] BET analysis revealed that the HA-IrO_x catalyst exhibits a high specific surface area of 97.3 m^2 g^{-1} (Fig. 1c), owing to its small particle size and rough surface structure. The value is five times larger than that of R-IrO_2 (20.8 m^2 g^{-1}) and three times larger than that of another amorphous catalyst, a-IrO_x (31.3 m^2 g^{-1}) (Fig. S1b†), implying the superior kinetic properties of HA-IrO_x. In electronic analysis using XPS, the Ir 4f spectra (Fig. S1c and S2a†) indicated that the heat treatment stabilized the Ir^{3+} state of a-IrO_x to Ir^{4+}; therefore, R-IrO_2 predominantly existed in the IrO_2 state with Ir^{4+} signals at 61.9 and 64.9 eV. The HA-IrO_x

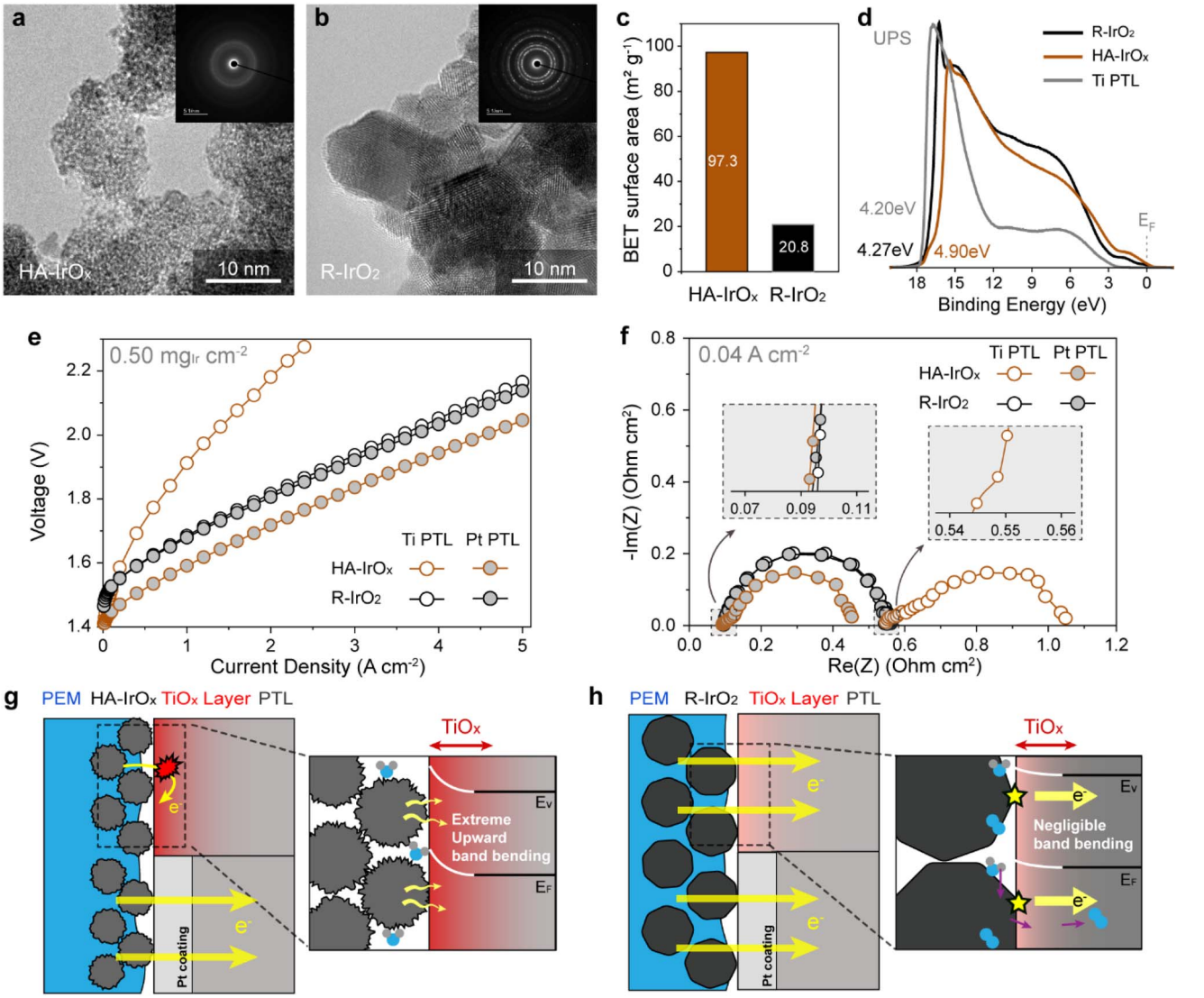

Fig. 1 Structural characterizations of the HA-IrO_x and R-IrO_2 catalysts and their effects on the single-cell anode interface (a and b) TEM images of the (a) HA-IrO_x and (b) R-IrO_2 catalysts with the insets of SAED pattern images. (c) Microstructure comparison of the catalysts using BET methods. (d) UPS spectra of the catalysts and bare Ti PTL and their work functions. (e and f) Single-cell analysis of the HA-IrO_x and R-IrO_2 anodes depending on the Pt coating. (e) IV polarization curves and (f) Nyquist plots of electrochemical impedance at 0.04 A cm^{-2}. (g and h) Schematic representations illustrating the TiO_x interfaces in the (g) HA-IrO_x and (h) R-IrO_2 anodes.

spectrum showed Ir^{3+} peaks at 62.3 and 65.3 eV, reflecting its amorphous nature. The XRD patterns displayed in Fig. S1d and S2b† show sharp peaks for R-IrO_2 and broad peaks for HA-IrO_x, highlighting the highly crystalline R-IrO_2 and amorphous HA-IrO_x structures.

The catalysts were further subjected to UPS analysis to estimate their interfacial properties with TiO_x. The UPS plots in Fig. 1d and S1e† revealed that HA-IrO_x has a work function of 4.90 eV, which decreases to 4.62 eV for a-IrO_x and 4.27 eV for R-IrO_2. These results suggest that a higher degree of amorphousness of iridium oxides is correlated with an increased work function. Because a larger gap in the work functions induces greater band bending at the semiconductor interface, the HA-IrO_x/TiO_x contact is likely to be the most susceptible to the electron transport problem. Notably, the TiO_x layer of the Ti PTL in our study exhibited a work function of 4.20 eV, which was much smaller than those of the HA-IrO_x and a-IrO_x catalysts and comparable to that of R-IrO_2.[41] Therefore, the greater amorphousness or higher catalytic activity of IrO_x is expected to impede the electron transport at the TiO_x interface.

The interface properties of the catalysts were evaluated using single-cell analysis.[42,43] Two catalysts, HA-IrO_x and R-IrO_2, were prepared as anode CLs at loading of 0.50 mg_{Ir} cm^{-2}. By comparing the electrochemical data with and without a 200 nm Pt coating on the PTL, TiO_x effects at each catalyst interface were investigated. As shown in the IV polarization curves of Fig. 1e, the HA-IrO_x anodes manifested a considerable difference between the two polarization curves; the Pt coating led to a remarkable performance improvement, quadrupling the current density from 0.65 to 2.70 A cm^{-2} at 1.8 V. This is in

sharp contrast to the R-IrO_2 anodes, which showed nearly identical single-cell performances regardless of the Pt coating. These results imply that a severe problem occurred in the HA-IrO_x anode because of TiO_x, whereas it disappeared in the R-IrO_2 case.

The different TiO_x properties are also evident in the Nyquist plots (Fig. 1f) of the electrochemical impedance spectrum (EIS) at 0.04 A cm^{-2}. The Nyquist plots were also fitted using equivalent circuits, as shown in Fig. S3,† to further analyze the impedance components. The specific equivalent circuit models used for each case are displayed in the corresponding insets of the plots. The HA-IrO_x anodes exhibited substantial differences in the high-frequency impedances depending on the PTL type. For the Pt-coated anode, the high-frequency impedance showed a reasonable *x*-axis intercept (R_{ohm}) at 0.088 ohm cm^2. However, for the bare Ti PTL case, the intercept value markedly increased to 0.528 ohm cm^2, and an additional semicircle ($R_{contact}$) appeared at 15 kHz, indicating the severely retarded electron transport. Conversely, the R-IrO_2 anodes made consistent impedance signals regardless of the PTL type, and their ohmic resistances were almost identical to 0.094–0.097 ohm cm^2, implying excellent electron transport not affected by TiO_x.

Notably, the intrinsic electrical conductivity of the catalysts was not a key contributor to the ohmic resistance. This is evident from the impedance comparison of the two Pt-coated anodes (Fig. 1f), where R_{ohm} of HA-IrO_x was slightly smaller than that of R-IrO_2. This is contrary to the general assumption that the crystalline rutile phases of iridium oxide have higher conductivities than their amorphous phases. However, the different intrinsic conductivities are dictated by the CL resistance (R_{CL}), as shown by the EIS analysis at a non-faradaic voltage of 1.35 V (Fig. S4a†).[44,45] The HA-IrO_x anode formed a constant phase element (CPE) in the frequency range of 4600–68 Hz, which stemmed from inefficient charge transport through the nonuniform and tortuous CL structure. By contrast, the CPE signal was absent, and nearly absolute capacitance signals appeared in the R-IrO_2 case, reflecting its high electrical conductivity. In this regard, we believe that the interfacial properties of TiO_x are a critical reason for the different ohmic resistances.

As mentioned above, the work functions of the catalysts are key factors in determining the TiO_x interface properties. This is illustrated schematically in Fig. 1g and h. In the case of HA-IrO_x (Fig. 1g), the work function mismatch at the interface may lead to a Schottky contact and severe band bending in TiO_x. Considering the work function difference between HA-IrO_x and TiO_x, the electron transport barrier was expected to reach 0.6 eV. However, because the difference is negligible for the R-IrO_2/TiO_x interface (~0.07 eV), it is believed that the R-IrO_2 anode does not develop a critical Schottky contact at the interface, enabling efficient electron transport through TiO_x (Fig. 1h).

Another speculation is associated with the amorphousness of the iridium oxides. The Ir L-edge spectra of *in situ* X-ray absorption near-edge spectroscopy (XANES) experiments in Fig. S5† show that the white-line peaks of the two catalysts behave differently with the applied potential.[36] During a potential increase from 1.0 to 1.8 V, the white lines of R-IrO_2 did not change at all (Fig. S5a†). By contrast, the white lines of HA-IrO_x show a positive shift from 11 219 to 11 220 eV (Fig. S5b†), which is close to the increase in one d-band hole of Ir reported in previous studies. We inferred that positive charges easily accumulated in the HA-IrO_x catalysts because of the unclear boundaries between the particles. In such cases, the accumulated positive charges may spread to neighboring TiO_x, leading to electron depletion and deteriorated electrical conductivity.

Despite its excellent electron transport properties, the R-IrO_2 catalyst exhibited poor single-cell performance owing to its inherently low catalytic activity compared to HA-IrO_x as predicted by TEM, BET, and XPS analyses. The Tafel plots in Fig. S4b,† extracted from the single-cell polarization data, show that the HA-IrO_x anode has a lower onset potential than R-IrO_2. Moreover, the Tafel slopes of the Pt-coated anodes were 38.0 and 53.5 mV dec^{-1} for HA-IrO_x and R-IrO_2, respectively, probably owing to different reaction mechanisms for the two catalysts (*i.e.*, lattice oxygen evolution mechanism *versus* adsorbate evolution mechanism). The crystalline rutile structure and large particle size are the main reasons for the large activation polarization for the R-IrO_2 anode, and the comparison of the two catalyst anodes coupled with the Pt-coated PTL presents that the current density for R-IrO_2, which is 2.0 A cm^{-2} at 1.8 V, is 25% smaller than that for the HA-IrO_x anode (2.7 A cm^{-2}).

The overall single-cell characteristics with varying catalysts and PTL types are summarized in the overpotential breakdown results in Fig. S6.† These results indicate that the physical properties of the iridium oxide catalyst play an important role in controlling the TiO_x interface, but this results in a trade-off with the catalytic activity. Notwithstanding its high catalytic activity, HA-IrO_x suffered significant performance problems when coupled with a bare Ti PTL. However, despite their high electrical conductivity, the R-IrO_2 anodes exhibited comparatively low performance owing to their large activation polarization. This indicates that achieving high catalytic activity along with outstanding electrical conductivity at the CL/PTL interface is crucial for maximizing PEMWE single-cell performance.

3.2. Fabrication and analysis of double-layered catalyst layer

Industry and researchers currently employ Pt-coated PTLs to overcome the limitations of electron transport in high-activity IrO_x anodes; however, the high material and manufacturing costs of Pt coatings pose a significant economic burden for commercialization. Specifically, the mostly used commercial 200 nm coating corresponds to 0.43 mg_{Pt} cm^{-2}, which should be decreased or eliminated to reduce overall stack price. In this context, we propose a double-layered CL (DL-CL), which is a combination of the distinct layers of two catalysts (HA-IrO_x and R-IrO_2), as a simple and effective anode structure that exhibits both high performance and cost efficiency. In the DL-CL, the minimum amount of R-IrO_2 was placed at the Ti PTL interface, whereas HA-IrO_x with a dominant portion of the total iridium loading was positioned on the opposite side, as illustrated in Fig. 2a. This structure was intended to secure efficient interface electron transport by inserting the R-IrO_2 catalyst at the CL/PTL interface while ensuring that the HA-IrO_x catalysts

actively participated in the OER near the membrane, not affected by TiO_x.

The DL-CL was fabricated in two steps. First, the HA-IrO_x CL was prepared *via* ball milling and doctor blade coating. The prepared HA-IrO_x CL, coupled with the cathode CL, was transferred to a membrane *via* decal transfer. Subsequently, the R-IrO_2 slurry was spray-coated directly onto the HA-IrO_x side of the CCM (Fig. S7†). The cross-sectional SEM image in Fig. 2b demonstrates a double-layered structure: a dense HA-IrO_x CL and a comparatively porous R-IrO_2 CL. Although the catalyst loadings of HA-IrO_x and R-IrO_2 were controlled to 0.30 and 0.20 mg_{Ir} cm^{-2}, respectively, the two CLs featured similar thicknesses within the 1.17–1.18 μm range owing to the different porosities. This difference is corroborated by the high-magnification SEM images (Fig. S8†). Presumably, the smaller size of HA-IrO_x forces more aggregation of the primary particles owing to stronger van der Waals interactions, resulting in smaller pores and lower porosity compared to R-IrO_2. This is consistent with the Barrett–Joyner–Halenda analysis shown in Fig. S2c,† where the HA-IrO_x particles possess only micropores with a size distribution of 2–20 nm, while R-IrO_2 also had macropores larger than 100 nm.

The DL-CL was then applied to a single-cell anode, and its performance was compared with that of other CLs. When using the bare Ti PTLs, the DL-CL anode exhibited remarkably higher current densities compared to the single-layered CLs, as shown in Fig. 2c; the current density of DL-CL at 1.8 V was 340% higher than that of HA-IrO_x CL and 55% higher than that of R-IrO_2. The Nyquist plots in Fig. 2d and their equivalent circuit analysis in Fig. S9† show that the low ohmic resistance and small low-frequency semicircle (R_{ct}) account for the superior performance of the DL-CL anode. Importantly, the ohmic resistance was as low as that of R-IrO_2 at ~0.08 ohm cm^2, and the R_{ct} was comparable to that of HA-IrO_x, indicating that DL-CL combined the advantages of two catalyst anodes. In addition, the single-cell performance of the DL-CL anode did not change even without the Pt coating, as shown in the IV polarization curves in Fig. S10a.† The difference between the two DL-CL anodes was also negligible in the Nyquist plots (Fig. S10b†), highlighting the role of the R-IrO_2 layer in stabilizing the TiO_x interface. To clarify whether the fabrication method contributes to the improvement or not, we also characterized the single-layered CCMs of HA-IrO_x and R-IrO_2 prepared *via* the spray-coating method. The IV polarization and EIS results in Fig. S11† demonstrated that the spray-coating method did not notably enhance the performance compared to the decal-transferred method. Rather, the HA-IrO_x sample showed a hugely deteriorated performance for the spray-coated case. These data indicate that the fabrication methods are not the critical contributors determining the DL-CL performance.

Interestingly, the DL-CL performed better than the HA-IrO_x anode with the Pt-coated PTL (Fig. S10a†). Considering the similar ohmic and kinetic resistances (Fig. S10b†), we ascribed this enhancement to efficient charge transport through the DL-CL. This was supported by the non-faradaic impedance analysis results shown in Fig. S10c,† where the R_{CL} of DL-CL was nearly half that of HA-IrO_x. The highly conductive R-IrO_2 layer appeared to increase the overall electrical conductivity, leading

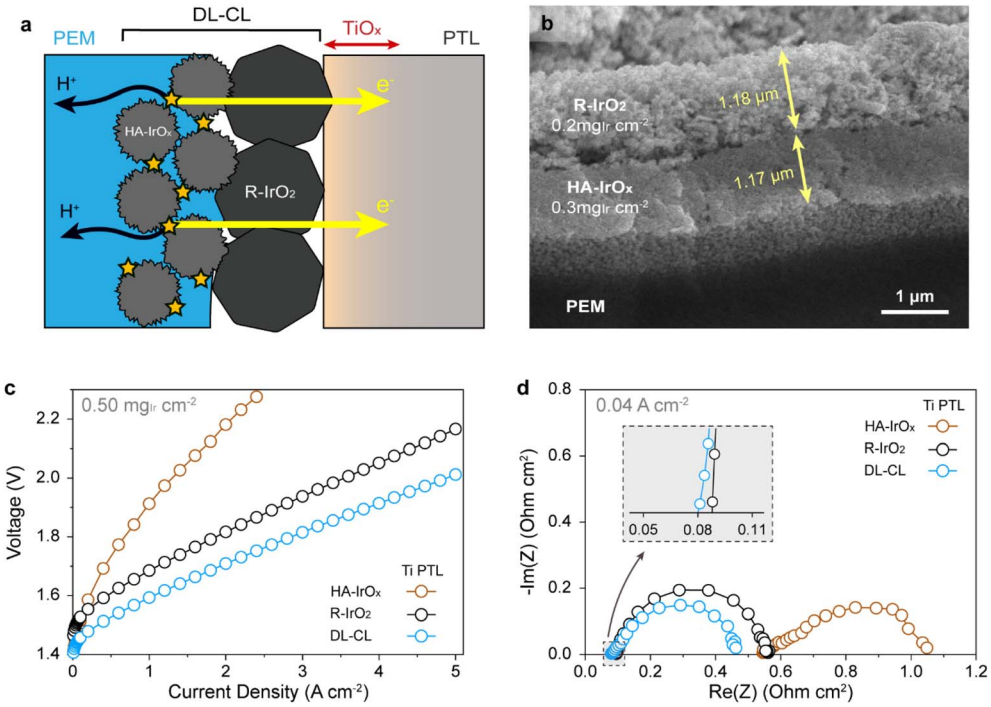

Fig. 2 Superior single-cell performance of the double-layered catalyst layer (DL-CL). (a) Schematic of the DL-CL/TiO_x interface, enabling efficient electron transport. (b) Cross-sectional SEM image of the DL-CL CCM. (c) and (d) Single-cell data comparisons of the DL-CL, HA-IrO_x, and R-IrO_2 anodes that were coupled with the bare Ti PTLs. (c) IV polarization curves and (d) Nyquist plots at 0.04 A cm^{-2}.

to performance enhancement, especially in the high-current-density region.

The Tafel plots in Fig. S10d† compare the kinetic performance of DL-CL with the HA-IrO_x anodes of two different loadings (0.30 and 0.50 mg_{Ir} cm^{-2}). The DL–CL plot is located in the middle of the two HA-IrO_x anodes because of the presence of low-activity R-IrO_2 catalysts. However, because the R-IrO_2 fraction of the total 0.50 mg_{Ir} cm^{-2} was relatively small, the loss in kinetic performance was also not significant, and the onset potential and Tafel slope of the DL-CL were comparable to those of the HA-IrO_x anodes with 0.50 mg_{Ir} cm^{-2} loading. These results demonstrated that the double-layered structure effectively retained the high activity of the HA-IrO_x catalyst.

Notably, the R-IrO_2 layer was significantly less compact than the Pt coating. According to the SEM image, an R-IrO_2 layer with 1 mg_{Ir} cm^{-2} exhibits a thickness of 5.9 μm, which is 12 times larger than the theoretical thickness (0.47 μm (mg_{Pt} cm^{-2})$^{-1}$) of the dense Pt coating. Therefore, the R-IrO_2 layer was much thicker at the same PGM loading, making it more effective at separating the IrO_x catalysts from the TiO_x interface. This was further verified through single-cell experiments with varying R-IrO_2 content in the DL-CL (Fig. S12†), where reducing the loading to 0.05 mg_{Ir} cm^{-2} in the DL-CL did not cause a performance drop or an increase in the ohmic resistance. The sustained high performance at such a low loading highlights the effectiveness of the R-IrO_2 layer, given that the PGM content is only one-eighth that of the commercial Pt coating (0.05 mg_{Ir} cm^{-2} *vs.* 0.43 mg_{Pt} cm^{-2}). The 0.05 mg_{Ir} cm^{-2} loading is even lower than the minimum Pt-coating loading (0.10 mg_{Pt} cm^{-2}) required to ensure high IrO_x anode performance, as reported by Geuß *et al.*[46] In addition, the high porosity of the R-IrO_2 layer is believed to facilitate oxygen, water, and electron transport through the CL (Fig. S10c†), which functions similarly to a microporous layer.

3.3. Structure effects of double-layered catalyst layer

To further identify the origin of the superior electrochemical performance of the DL-CL anodes, another double-layered CL with an inverted arrangement of the catalysts was fabricated in the same manner as the DL-CL. The inverted DL-CL (IDL-CL) structure is illustrated in Fig. 3a, and the HA-IrO_x CL is placed at the PTL interface with the R-IrO_2 CL on the PEM side. The catalyst loading and composition were the same as those of the DL-CL, and only the structure was reversed. The cross-sectional and surface SEM images shown in Fig. S13† demonstrate an inverted arrangement with a dense HA-IrO_x CL on top and a porous R-IrO_2 CL adjacent to the membrane. If the double-layered structure is the primary reason for the outstanding performance of the original DL-CL, the IDL-CL anode should exhibit an equally high performance. Otherwise, the catalyst arrangement was the dominant factor.

The single-cell analyses shown in Fig. 3b and S14a–c† verified that the latter statement is correct. The IDL-CL anode exhibited extremely poor performance when coupled with the bare Ti PTL, and its performance was significantly dependent on the Pt coating. Unlike the decent cell performance with the Pt-coated PTL (2.62 A cm^{-2} at 1.8 V), the uncoated anode did not perform properly and showed abnormal voltage losses at low

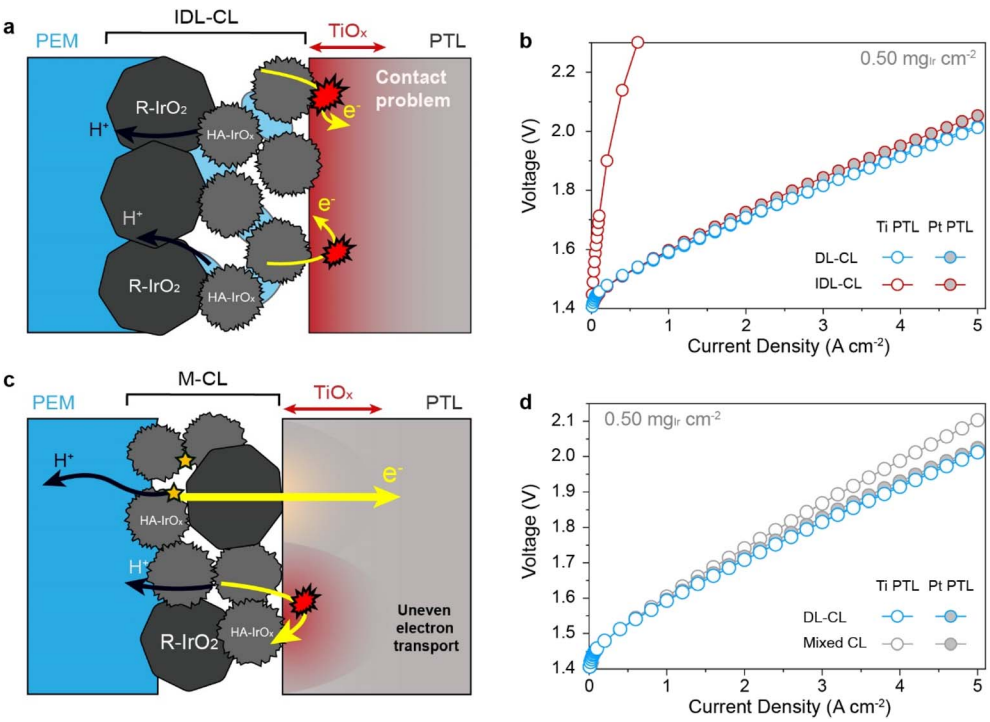

Fig. 3 Catalyst arrangement in DL-CL. (a) Schematic of the inverted DL-CL structure and its interface with TiO_x. (b) IV polarization curves of the DL-CL and IDL-CL anodes depending on the Pt coating. (c) Schematic of the M-CL anode. (d) IV polarization curves of the DL-CL and M-CL anodes depending on the Pt coating.

current densities (0.15 A cm^{-2} at 1.8 V) (Fig. 3b). The impedance analysis at 0.04 A cm^{-2} (Fig. S14a†) demonstrated that a large semicircle in the high-frequency region (63–40 Hz) accounted for the abnormal voltage loss. Because the IDL-CL anode with the Pt-coated PTL exhibited outstanding kinetic performance (Fig. S14b†) and small overpotentials (Fig. S14c†), which was comparable to that of the DL-CL anodes, the TiO_x interface was responsible for the performance deterioration of the uncoated anode. These results are analogous to the single-cell data of HA-IrO_x and contrary to the DL-CL anodes, indicating that the superior performance of the DL-CL is not owing to its double-layered structure, but is mostly attributable to the optimized catalyst arrangement.

To further understand the structural effect of the CL on the TiO_x interface, a mixed CL (M-CL) was prepared by homogeneously dispersing the HA-IrO_x and R-IrO_2 catalysts and then casting them into a single layer. The HA-IrO_x catalyst was used at 1.5 times the amount of R-IrO_2 to ensure the same catalyst ratio as that of DL-CL. Fig. 3c shows schematics of the M-CL structure and its interface with TiO_x. Assuming a uniform catalyst distribution in the M-CL, TiO_x was considered to form a mixed interface of the two catalysts, and single-cell analysis could reveal how the interface structure affects electron transport in TiO_x (Fig. 3d and S15†). When paired with the bare Ti PTL, the M-CL anode exhibited reasonable performance without the severe polarization observed in the HA-IrO_x and IDL-CL anodes. Electrochemical impedance analysis indicated that M-CL did not create a large high-frequency semicircle (Fig. S15a†). However, the overall performance was inferior to that of the DL-CL anode, and the ohmic resistance of the M-CL was 21% higher, implying contact resistance. An enlarged ohmic polarization of the M-CL anode was also observed in the overpotential breakdown analysis (Fig. S15b†), while the other polarizations were nearly the same as the DL-CL anode. In contrast, the M-CL anode exhibited a comparable performance and overpotentials to the DL-CL when the Pt-coated PTL was employed, suggesting that the M-CL was also affected by the presence of TiO_x. We ascribed this to the HA-IrO_x/TiO_x interface, partially formed at the CL/PTL contact, which caused partial band bending in TiO_x and reduced electrical conductivity. These investigations of the M-CL support the conclusion that setting HA-IrO_x apart from the TiO_x surface is crucial for interface engineering in Pt-coating-free anodes. The presence of R-IrO_2 in the anode CL was not sufficient to mitigate the interfacial resistance; however, the detrimental components should be completely removed from TiO_x to attain excellent electron transport.

3.4. Long-term durability test of the DL-CL/TiO_x interface

However, the eliminated TiO_x effect by the DL-CL has practical meaning only when this phenomenon persists for a long period of water electrolysis operation. Therefore, we conducted the long-term operation test of the DL-CL anode coupled with the bare Ti PTL at a constant current of 1 A cm^{-2} over 1000 h. HA-IrO_x anodes with and without the Pt coating were also tested for comparison. The catalyst loading and composition were controlled as described above for the single-cell analysis, whereas the NR212 membranes were changed to thicker N115 membranes to exclude membrane deformation during the test.

The chronological voltage profiles in Fig. 4a compare the three samples during constant-current operation. The HA-IrO_x anode with the bare Ti PTL made a rapid voltage increase of 1.43 mV h^{-1} and jumped above the safety voltage limit (2.15 V) within 80 h. A performance drop is also observed in the IV polarization curves (Fig. 4b), and the Nyquist plots of the impedance signals (Fig. 4c and S16†) indicate that the enlarged high-frequency semicircle is responsible for the rapid voltage increase. These results indicate that the insulation by TiO_x worsened during single-cell operation. We hypothesized that the thickening and/or increased amorphousness of the TiO_x layer would lead to a significant decrease in the electrical conductivity drop at the interface.

Conversely, the HA-IrO_x with the Pt-coated PTL underwent a relatively stable operation for 1000 h. A gradual voltage increase with a rate of 0.107 mV h^{-1} was observed, and the polarization curves and Nyquist plots showed that the degradation was associated with the decline in kinetic and mass transport properties. In particular, the change in R_{ct} at 0.04 A cm^{-2} was more noticeable than that in the ohmic resistance in the Nyquist plots (Fig. 4c). This implies that high electron conductivity was retained in the anode owing to the Pt coating, but there was considerable degradation in the catalyst and/or CL, leading to decreased kinetic properties and further increased transport polarization. These results are summarized in the overpotential analysis shown in Fig. S17.†

In the case of the DL-CL coupled with the bare Ti PTL, the voltage profile was stable over 1000 h of operation. Despite the absence of the Pt coating, the voltage degradation rate (0.097 mV h^{-1}) was even smaller than that of the Pt-coated HA-IrO_x anode. Surprisingly, the ohmic resistance in the Nyquist plot did not increase at all (Fig. 4c), indicating invariant TiO_x interface properties. Based on the breakdown of overpotentials shown in Fig. S17,† the kinetic and mass transport overpotentials were the primary reasons for the degradation. Given the similar degradation phenomenon of the Pt-coated HA-IrO_x anode, it was thought that the dissolution and/or destruction of the HA-IrO_x layer was the main contributor to the degradation of the two anodes. These align well with the previous publications that demonstrated the severe dissolution and/or agglomeration of the IrO_x catalyst, playing a critical role in the PEMWE degradation.[47–49] Although the degradation rate of the DL-CL was not impressive, when compared with that in publications, we would like to emphasize that the high retention ability of the excellent electron transport in the non-Pt-coated condition has not been presented previously; all the bare Ti PTL anodes, especially at low iridium loadings, resulted in huge ohmic resistance growth after the long-term operation, as shown in the HA-IrO_x data and results in numerous publications.[13,20,49,50] Although further investigation is required, R-IrO_2 at the PTL interface is also beneficial for preventing the structural deformation of TiO_x during the OER.

Taken together, the DL-CL anode exhibited excellent interface properties without any protective coating, lasting for a long-

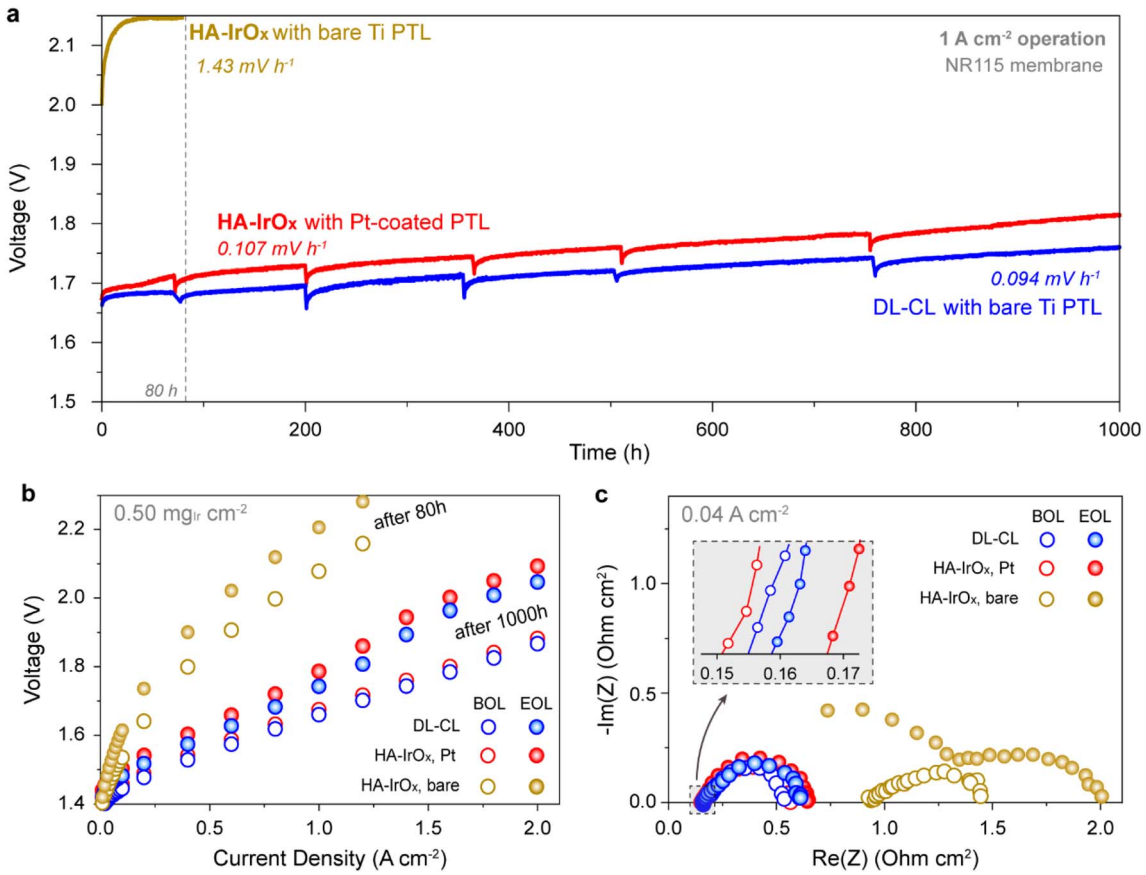

Fig. 4 Durability test of the DL-CL anode with the bare Ti PTL. (a) Voltage profiles of the constant current operation at 1 A cm^{-2} for the HA-IrO_x and DL-CL anodes. The bare Ti PTL was adopted for the DL-CL anode, and two HA-IrO_x anodes with and without the Pt coating were tested for comparison. (b and c) Single-cell characterizations before and after the operation. (b) IV polarization curves. (c) Nyquist plots of impedance signals at 0.04 A cm^{-2} with a magnified view in the inset.

term operation of 1000 h. We believe that this strategy can pave the way for achieving high-performance and cost-effective PEMWE by realizing a Pt-coating-free anode. Possible following works can be optimizing the DL-CL materials to achieve a lower degradation rate, exploring the reason for the high stability of the TiO_x interface, and suggesting practical methods for fabricating DL-CL anodes.

4 Conclusion

In summary, this study introduced a double-layered catalyst layer (DL-CL) that can effectively overcome electron transport limitations caused by TiO_x at the anode interface. Two catalyst layers were strategically combined, one with a low work function (R-IrO_2) and the other with a high-activity catalyst (HA-IrO_x), to fabricate a DL-CL anode with excellent electron conductivity without the need for the Pt coating. Compared to single-layered CLs, the DL-CL anode exhibited superior single-cell performance, even with a bare Ti PTL, owing to the significantly lower kinetic and ohmic overpotentials, demonstrating the synergistic effect of the R-IrO_2 and HA-IrO_x catalysts. Further investigations by varying the CL structures revealed that the key factor for performance improvement was the catalyst arrangement, highlighting the importance of positioning a high-work-function catalyst away from the TiO_x interface. A durability test further demonstrated that the DL-CL maintained a highly conductive TiO_x interface over 1000 h of operation, underlining its practical feasibility. Given the high cost and material demand of conventional Pt coatings (~200 nm or ~0.43 mg_{Pt} cm^{-2}), the DL-CL anode provides a promising alternative, replacing the Pt coating with a ultralow R-IrO_2 loading (~0.05 mg_{Ir} cm^{-2}). This study establishes DL-CL as a viable strategy for cost-effective and durable anode designs in PEMWE.

Data availability

The data supporting this article have been included as part of the ESI.†

Author contributions

D. Kim and G. Doo conceptualized the experiments and drafted the manuscript. D. Kim, G. H. Jung, Y. H. Yun, and S. An conducted the experimental work. J. Park, C. Lee, S. Lee, H. Park, S.-K. Kim, H.-S. Cho, and H.-T. Kim performed analyses and characterizations. N. Jung, G. Doo, and M. J. Kim supervised the

project and provided guidance through regular discussions. All authors reviewed the results and contributed to the manuscript.

Conflicts of interest

There are no conflicts to declare.

Acknowledgements

This research was supported by the National Research Foundation of Korea (NRF) Grant funded by the Korea Government (MSIT) (No. 2022M3H4A3A01083536) and the Technology Innovation Program (1415188335, Development of Membrane Electrode Assembly and stack components for PEM water electrolysis) funded by the Ministry of Trade, Industry & Energy (MOTIE, Korea). This work was also conducted under framework of the research and development program of the Korea Institute of Energy Research (C5-2407).

References

1 C. V. Pham, D. Escalera-López, K. Mayrhofer, S. Cherevko and S. Thiele, *Adv. Energy Mater.*, 2021, **11**, 2101998.
2 P. Shirvanian and F. van Berkel, *Electrochem. Commun.*, 2020, **114**, 106704.
3 W. H. Lee, Y.-J. Ko, J. H. Kim, C. H. Choi, K. H. Chae, H. Kim, Y. J. Hwang, B. K. Min, P. Strasser and H.-S. Oh, *Nat. Commun.*, 2021, **12**, 4271.
4 C. Van Pham, M. Bühler, J. Knöppel, M. Bierling, D. Seeberger, D. Escalera-López, K. J. Mayrhofer, S. Cherevko and S. Thiele, *Appl. Catal. B Environ.*, 2020, **269**, 118762.
5 M. Carmo, D. L. Fritz, J. Mergel and D. Stolten, *Int. J. Hydrogen Energy*, 2013, **38**, 4901–4934.
6 U. Babic, M. Suermann, F. N. Büchi, L. Gubler and T. J. Schmidt, *J. Electrochem. Soc.*, 2017, **164**, F387.
7 M. Schalenbach, G. Tjarks, M. Carmo, W. Lueke, M. Mueller and D. Stolten, *J. Electrochem. Soc.*, 2016, **163**, F3197.
8 N. Diklic, A. H. Clark, J. Herranz, J. S. Diercks, D. Aegerter, M. Nachtegaal, A. Beard and T. J. Schmidt, *ACS Energy Lett.*, 2022, **7**, 1735–1740.
9 S. Geiger, O. Kasian, B. R. Shrestha, A. M. Mingers, K. J. Mayrhofer and S. Cherevko, *J. Electrochem. Soc.*, 2016, **163**, F3132.
10 T. Lazaridis, B. M. Stühmeier, H. A. Gasteiger and H. A. El-Sayed, *Nat. Catal.*, 2022, **5**, 363–373.
11 C. Minke, M. Suermann, B. Bensmann and R. Hanke-Rauschenbach, *Int. J. Hydrogen Energy*, 2021, **46**, 23581–23590.
12 M. Bernt, A. Siebel and H. A. Gasteiger, *J. Electrochem. Soc.*, 2018, **165**, F305–F314.
13 C. Liu, M. Shviro, A. S. Gago, S. F. Zaccarine, G. Bender, P. Gazdzicki, T. Morawietz, I. Biswas, M. Rasinski and A. Everwand, *Adv. Energy Mater.*, 2021, **11**, 2002926.
14 Z. Kang, J. Mo, G. Yang, Y. Li, D. A. Talley, S. T. Retterer, D. A. Cullen, T. J. Toops, M. P. Brady and G. Bender, *Appl. Energy*, 2017, **206**, 983–990.
15 C. Rakousky, U. Reimer, K. Wippermann, M. Carmo, W. Lueke and D. Stolten, *J. Power Sources*, 2016, **326**, 120–128.
16 C. Liu, J. A. Wrubel, E. Padgett and G. Bender, *Appl. Energy*, 2024, **356**, 122274.
17 C. Liu, K. Wippermann, M. Rasinski, Y. Suo, M. Shviro, M. Carmo and W. Lehnert, *ACS Appl. Mater. Interfaces*, 2021, **13**, 16182–16196.
18 A. T. Mayyas, M. F. Ruth, B. S. Pivovar, G. Bender, and K. B. Wipke, *Manufacturing Cost Analysis for Proton Exchange Membrane Water Electrolyzers*, National Renewable Energy Laboratory (NREL), Golden, CO (United States), 2019.
19 J. Lopata, Z. Kang, J. Young, G. Bender, J. Weidner and S. Shimpalee, *J. Electrochem. Soc.*, 2020, **167**, 064507.
20 C. Liu, M. Shviro, G. Bender, A. S. Gago, T. Morawietz, M. J. Dzara, I. Biswas, P. Gazdzicki, Z. Kang and S. F. Zaccarine, *J. Electrochem. Soc.*, 2023, **170**, 034508.
21 M. Bernt, C. Schramm, J. Schröter, C. Gebauer, J. Byrknes, C. Eickes and H. Gasteiger, *J. Electrochem. Soc.*, 2021, **168**, 084513.
22 A. Hartig-Weiß, M. Bernt, A. Siebel and H. A. Gasteiger, *J. Electrochem. Soc.*, 2021, **168**, 114511.
23 U. Babic, E. Nilsson, A. Pătru, T. J. Schmidt and L. Gubler, *J. Electrochem. Soc.*, 2019, **166**, F214.
24 C. Rozain, E. Mayousse, N. Guillet and P. Millet, *Appl. Catal. B Environ.*, 2016, **182**, 123–131.
25 J. Mo, Z. Kang, S. T. Retterer, D. A. Cullen, T. J. Toops, J. B. Green Jr, M. M. Mench and F.-Y. Zhang, *Sci. Adv.*, 2016, **2**, e1600690.
26 T. Schuler, J. M. Ciccone, B. Krentscher, F. Marone, C. Peter, T. J. Schmidt and F. N. Büchi, *Adv. Energy Mater.*, 2020, **10**, 1903216.
27 G. Doo, J. Park, J. Park, J. Heo, J. Jung, D. W. Lee, H. Bae, J. Hyun, E. Oh and J. Kwen, *ACS Energy Lett.*, 2023, **8**, 2214–2220.
28 W. Yang, T. Moehl, E. Service and S. D. Tilley, *Adv. Energy Mater.*, 2021, **11**, 2003569.
29 A. G. Scheuermann, J. P. Lawrence, K. W. Kemp, T. Ito, A. Walsh, C. E. Chidsey, P. K. Hurley and P. C. McIntyre, *Nat. Mater.*, 2016, **15**, 99–105.
30 G. Doo, H. Bae, J. Park, J. Hyun, I. Kim, D. W. Lee, E. Oh and H.-T. Kim, *ACS Nano*, 2024, **18**, 23331–23340.
31 F. Hegge, F. Lombeck, E. Cruz Ortiz, L. Bohn, M. von Holst, M. Kroschel, J. Hübner, M. Breitwieser, P. Strasser and S. Vierrath, *ACS Appl. Energy Mater.*, 2020, **3**, 8276–8284.
32 Y. Qiu, H. Zhang, H. Zhong and F. Zhang, *Int. J. Hydrogen Energy*, 2013, **38**, 5836–5844.
33 M. Povia, D. F. Abbott, J. Herranz, A. Heinritz, D. Lebedev, B.-J. Kim, E. Fabbri, A. Patru, J. Kohlbrecher and R. Schäublin, *Energy Environ. Sci.*, 2019, **12**, 3038–3052.
34 J. Gao, C.-Q. Xu, S.-F. Hung, W. Liu, W. Cai, Z. Zeng, C. Jia, H. M. Chen, H. Xiao and J. Li, *J. Am. Chem. Soc.*, 2019, **141**, 3014–3023.
35 V. Pfeifer, T. Jones, J. V. Vélez, C. Massué, M. Greiner, R. Arrigo, D. Teschner, F. Girgsdies, M. Scherzer and J. Allan, *Phys. Chem. Chem. Phys.*, 2016, **18**, 2292–2296.

36 D. F. Abbott, D. Lebedev, K. Waltar, M. Povia, M. Nachtegaal, E. Fabbri, C. Copéret and T. J. Schmidt, *Chem. Mater.*, 2016, **28**, 6591–6604.
37 F. Karimi, A. Bazylak and B. A. Peppley, *J. Electrochem. Soc.*, 2017, **164**, F464.
38 B. Hasa, U. R. Aryal, S. Higashi, N. E. Tolouei, J. T. Lang, B. Erb, A. Smeltz, I. V. Zenyuk and G. Zhu, *Appl. Catal. B Environ. Energy*, 2025, **361**, 124616.
39 J. P. H. Li, X. Zhou, Y. Pang, L. Zhu, E. I. Vovk, L. Cong, A. P. van Bavel, S. Li and Y. Yang, *Phys. Chem. Chem. Phys.*, 2019, **21**, 22351–22358.
40 J. F. Moulder, W. F. Stickle, P. E. Sobol and K. D. Bomben, *Handbook of X-ray Photoelectron Spectroscopy*, Perkin-Elmer Corporation, Eden Prairie, 1992.
41 S. Kashiwaya, J. Morasch, V. Streibel, T. Toupance, W. Jaegermann and A. Klein, *Surfaces*, 2018, **1**, 73–89.
42 S. Chatterjee, X. Peng, S. Intikhab, G. Zeng, N. N. Kariuki, D. J. Myers, N. Danilovic and J. Snyder, *Adv. Energy Mater.*, 2021, **11**, 2101438.
43 M. Bernt, J. Schröter, M. Möckl and H. Gasteiger, *J. Electrochem. Soc.*, 2020, **167**, 124502.
44 U. Babic, T. J. Schmidt and L. Gubler, *J. Electrochem. Soc.*, 2018, **165**, J3016.
45 E. Padgett, G. Bender, A. Haug, K. Lewinski, F. Sun, H. Yu, D. A. Cullen, A. J. Steinbach and S. M. Alia, *J. Electrochem. Soc.*, 2023, **170**, 084512.
46 M. Geuß, L. Löttert, A. Hutzler, J. Schwarz, J. Nováková, I. Khalakhan, M. Gaberšček, K. J. Mayrhofer, S. Thiele and S. Cherevko, *Chem. Eng. J.*, 2025, 162887.
47 Z. Zeng, R. Ouimet, L. Bonville, A. Niedzwiecki, C. Capuano, K. Ayers, A. P. Soleymani, J. Jankovic, H. Yu and G. Mirshekari, *J. Electrochem. Soc.*, 2022, **169**, 054536.
48 M. Möckl, M. F. Ernst, M. Kornherr, F. Allebrod, M. Bernt, J. Byrknes, C. Eickes, C. Gebauer, A. Moskovtseva and H. A. Gasteiger, *J. Electrochem. Soc.*, 2022, **169**, 064505.
49 A. Voronova, S. Kim, D. Kim, H.-Y. Park, J. H. Jang and B. Seo, *Energy Environ. Sci.*, 2023, **16**, 5170–5184.
50 A. J. McLeod, L. V. Bühre, B. Bensmann, O. E. Herrera and W. Mérida, *J. Power Sources*, 2024, **589**, 233750.